

Full paper



Strong anisotropic transport properties of quasi-one-dimensional ZrTe₃ nanoribbons

Seonhye Youn^{a,1}, Jeongmin Kim^{b,1}, Heejun Lee^c, Dong Hwan Kim^b, Joonho Bang^{c,d,*},
Wooyoung Lee^{a,**}

^a Department of Materials Science and Engineering, Yonsei University, 50 Yonsei-ro, Seodaemun-gu, Seoul 03722, South Korea

^b Division of Nanotechnology, DGIST, 333 Techno Jungang-daero, Hyeonpung-eup, Dalseong-gun, Daegu 42988, South Korea

^c School of Materials Science and Engineering, Gyeongsang National University, Jinju 52828, South Korea

^d Department of Materials Engineering and Convergence Technology, Gyeongsang National University, Jinju 52828, South Korea

ARTICLE INFO

Keywords:

ZrTe₃
Transition metal trichalcogenide
Quasi-one-dimensional structure
Anisotropic transport
Seebeck coefficient
Electrical conductivity

ABSTRACT

Transition metal trichalcogenides (TMTCs) with quasi-one-dimensional (quasi-1D) structures have attracted extensive interest in diverse fields because of their unique electronic properties. Herein, we report strong in-plane anisotropic transport properties of ZrTe₃ nanoribbons, which originate from their quasi-1D structures. ZrTe₃ nanoribbons were mechanically exfoliated from bulk single crystals, and transport properties, including electrical conductivity (σ) and Seebeck coefficient (S), were measured in the longitudinal and transverse directions of the rectangular nanoribbons. σ was higher in the transverse direction than that in the longitudinal direction. S measurement revealed further clear anisotropic characteristics, and positive and negative S values were obtained in the longitudinal and transverse directions, respectively. Furthermore, a significant change in the transport properties was observed with a post treatment, and the potential of ZrTe₃ for transport property modulation was confirmed. We believe that our findings will contribute to the understanding of anisotropic transport in quasi-1D ZrTe₃ and expansion of the application fields of quasi-1D ZrTe₃.

1. Introduction

In the past few decades, two-dimensional (2D) materials, such as graphene, transition metal dichalcogenides (TMDCs), and black phosphorus have received considerable attention owing to their extraordinary potentials for various applications.[1–3] Specifically, TMDCs have become the focus of research on 2D materials due to their strong chemical stabilities, tunable band structures, high charge-carrier mobilities, and excellent optical, electronic, mechanical, and physical properties.[4–12]

Recently, transition metal trichalcogenides (TMTCs), denoted as MX₃ (where M = Zr, Ti, and other transition metals and X = Te, S, or Se), have garnered significant attention because of their robust in-plane anisotropic transport properties arising from their quasi-one-dimensional (quasi-1D) structures.[13] Similar to other 2D structures, TMTCs with layered structures stacked by weak van der Waals (vdW) forces can be exfoliated into 2D nanoribbons.[14] Particularly, TMTCs

are linked by strong covalent bonds along the quasi-1D chain direction and weak covalent bonds between adjacent chains.[14] Consequently, due to their unique structural features, TMTCs offer the advantages of both 2D and quasi-1D materials. TMTCs with quasi-1D structures exhibit several outstanding properties including peculiar charge density waves, superconductivity, and magnetic and thermoelectric properties, which can be utilized in nanoelectronic devices.[14,15]

The previous theoretical studies conducted on monolayer TiS₃ have reported the indirect-to-direct band gap transition and highly anisotropic electron mobility along the 1D chain direction, which is expected to be even higher than that of a MoS₂ monolayer.[14,16,17] In theoretical studies on ZrS₃, the first-principles calculations of bulk and monolayer structures have demonstrated robust in-plane anisotropic behaviors of electronic and thermal transport properties.[18] In contrast, ZrTe₃ with metallic characteristics different from those of other TMTCs has been extensively investigated because of its charge-density wave state at 63 K and superconductivity below 2 K.[13,19–23]

* Corresponding author at: School of Materials Science and Engineering, Gyeongsang National University, Jinju 52828, South Korea.

** Corresponding author.

E-mail addresses: bang@gnu.ac.kr (J. Bang), wooyoung@yonsei.ac.kr (W. Lee).

¹ S. Youn and J. Kim contributed equally to this work.

Interestingly, even in metallic ZrTe_3 , the anisotropic electron transport was theoretically predicted, and 1D chain direction-dependent electrical resistivity (ρ) and Seebeck coefficient (S) were observed in plate-like single crystals.[24] Moreover, thermal conductivity in the chain direction was expected to be higher than that in the direction normal to the chain direction.[14,25] However, despite the numerous theoretical predictions on the anisotropic transport properties of ZrTe_3 , only a few studies have successfully demonstrated these properties experimentally, and studies on exfoliated ZrTe_3 2D nanoribbons have rarely been reported.

Herein, we investigated the strong in-plane anisotropic transport properties of mechanically exfoliated ZrTe_3 nanoribbons. S values of the ZrTe_3 nanoribbons in the 1D chain direction were substantially different from those in the direction normal to the 1D chain direction, which were p - and n -type, respectively. The electrical conductivity (σ) along the direction normal to the 1D chain direction was higher than that along the 1D chain direction. The bidirectional measurements were conducted based on a single nanoribbon using microdevices to accurately evaluate the anisotropy of transport properties. Furthermore, the transport properties significantly changed with respect to the device process, which indicated the potential of ZrTe_3 for transport property modulation. Additionally, we theoretically calculated the band structure and transport properties of ZrTe_3 to confirm the anisotropies in σ and S .

2. Results and discussion

2.1. Structural characterizations of ZrTe_3 nanoribbons

ZrTe_3 crystallizes in a layered monoclinic structure belonging to the $P21/m$ (No.11) space group.[26–29] Fig. 1a depicts different views of the crystal structure of monolayer ZrTe_3 . The first dimension of ZrTe_3 originates from infinite MX_3 prismatic chains parallel to the y -axis, consisting of a Zr atom and six adjacent Te atoms. The prismatic chains form a monolayer structure via $M-X$ interchain bonds, leading to the second dimension along the x -axis. Interchain $M-X$ bonds are slightly longer than the intrachain $M-X$ bonds, and a Zr atom exists in effective eight-coordination in the monolayer structure.[24] ZrTe_3 monolayers are stacked on each other, producing multilayered crystals, resulting in the third dimension along the z -axis. ZrTe_3 crystal was exfoliated into rectangular ribbons with long length in the y -axis due to their quasi-1D structures with strong intrachain $M-X$ bonds (Fig. 1b and S1). Fig. 1c shows a high-resolution transmission electron microscopy (TEM) image of a ZrTe_3 nanoribbon in an x - y plane, which reveals the single-crystalline nature of the nanoribbon. The corresponding selected area electron diffraction (SAED) pattern exhibited clear diffraction spots of (100) and (010) planes (Fig. 1c inset). The lattice constants a and b were determined to be 5.88 and 3.96 Å from the (100) and (001) spots, respectively, which are in suitable agreement with those reported in previous studies.[27,30–33] To verify the crystal and stacking structures in the ZrTe_3 nanoribbon along the z -axis, we

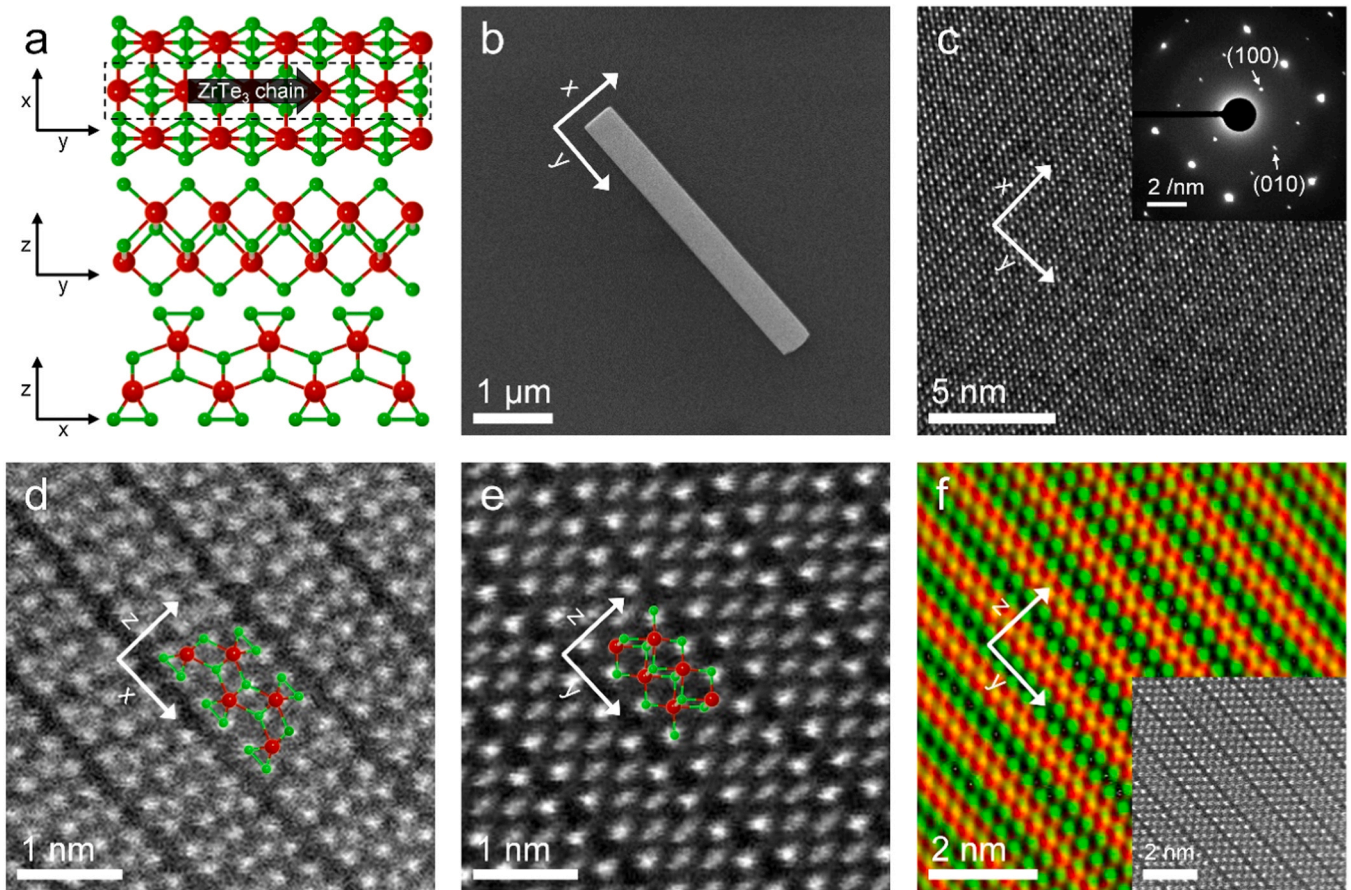


Fig. 1. Crystal structure of the ZrTe_3 nanoribbon. (a) Schematic of the crystal structure of monolayer ZrTe_3 with different views (x - y , y - z , and x - z planes). Red and green spheres represent Zr and Te atoms, respectively. Dashed-line rectangle indicates a prismatic chain of ZrTe_3 . (b) Scanning electron microscopy image of a mechanically exfoliated ZrTe_3 nanoribbon. (c) High-resolution transmission electron microscopy (TEM) image of a ZrTe_3 nanoribbon; inset depicts the corresponding selected area electron diffraction pattern along the [001] zone axis. (d and e) Cross-sectional scanning TEM (STEM) images of a ZrTe_3 nanoribbon representing atomic arrangements in the (d) x - z and (e) y - z planes. (f) TEM-energy-dispersive X-ray spectroscopy elemental mapping analysis of the y - z plane (Zr: red and Te: green); inset shows the corresponding STEM image.

prepared vertically sliced specimens using focused ion beam (FIB), and their cross-sectional scanning TEM (STEM) images demonstrated the atomic arrangements in the x - z and y - z planes (Fig. 1d and e). Atomic arrangement in the x - z plane clearly indicates triangular prismatic chain structures with three Te atoms coordinated around a Zr atom and inversely connected chains comprising a ZrTe_3 monolayer. Adjacent chain arrangement shifted along the y -axis and M-X interchain bonding structure were further evidently noticed in the y - z plane. Consequently, the ZrTe_3 monolayer was covered with Te atoms exposed on both top and bottom sides, and stacked nanoribbons were generated via weak vdW bonds between these Te atoms (Fig. 1f and S2). From the STEM images, the stacking distance (c) along the z -axis was evaluated to be 10.06 Å, which was consistent with those reported in previous studies. [31–34]

2.2. Chemical characterizations of ZrTe_3 nanoribbons

Fig. 2a and b depict the X-ray photoelectron spectra of Zr 3d and Te 3d, respectively. For the analyses of Zr 3d peaks, two sets of doublets, located at 180.4 eV ($3d_{5/2}$) and 182.8 eV ($3d_{3/2}$) and at 183 eV ($3d_{5/2}$) and 185.4 eV ($3d_{3/2}$), with a spin-orbit splitting of 2.4 eV were deconvoluted after background subtraction (Fig. 2a). Additionally, Zr^{4+} (the doublets detected in the high-binding energy region) and Zr^{2+} (the doublets located in the low-binding energy region) might coexist due to mixed chemical states in ZrTe_3 nanoribbons. [35] Moreover, three sets of doublets with a spin-orbit splitting of 10.4 eV were detected at 572.5 eV ($3d_{5/2}$) and 582.9 eV ($3d_{3/2}$), 571.7 eV ($3d_{5/2}$) and 582.1 eV ($3d_{3/2}$), and 573.2 eV ($3d_{5/2}$) and 583.6 eV ($3d_{3/2}$) after background subtraction (Fig. 2b). The respective peaks were assigned to the Zr-Te bonds (Te

atoms at the corners), Zr-Te bonds (Te atoms in neighboring chains), and Te-Te bonds. We also observed peaks at 576 and 586.4 eV corresponding to the Te-O bond originating from oxidized Te on the sample surface. These X-ray photoelectron spectroscopy (XPS) results are quite similar to those reported in previous studies. [28,35,36]

Raman spectra of ZrTe_3 nanoribbons were acquired by Raman spectroscopy using a 532 nm excitation laser at room temperature (Fig. 2c). Herein, four Raman peaks were noticed at 84.4, 105.9, 142.9, and 214.3 cm^{-1} , and the phonon mode of each peak is Ag with atomic movement in the x - z plane. [27,37] Furthermore, we characterized the crystal structures through X-ray diffraction (XRD) based on the bulk single crystals. The XRD pattern exhibited peaks at 8.82°, 17.66°, 26.68°, 27.54°, 35.86°, and 45.26°, which belong to the (001), (002), (003), (110), (004), and (005) planes, respectively, according to the standard PDF card (PDF# 80-2224) (Fig. 2d). [19,36,38] Atomic force microscopy (AFM) revealed the thicknesses and surface characteristics of the mechanically exfoliated ZrTe_3 nanoribbons for device fabrication (Fig. 2e and f). The height profiles demonstrated that the selected nanoribbons exhibited uniform surfaces and the thicknesses were determined to lie between 50–260 nm.

2.3. Anisotropic transport properties of ZrTe_3 nanoribbons

To confirm the anisotropic transport properties of the quasi-1D ZrTe_3 nanoribbons, σ and S were measured in the longitudinal (y -axis) and transverse (x -axis) directions of the rectangular ribbons (Fig. 3). FIB milling was employed to eliminate the mutual disturbance and long-length shape effect in the bidirectional measurement of a single nanoribbon (Fig. 3a). During the division of a single nanoribbon, an electron-

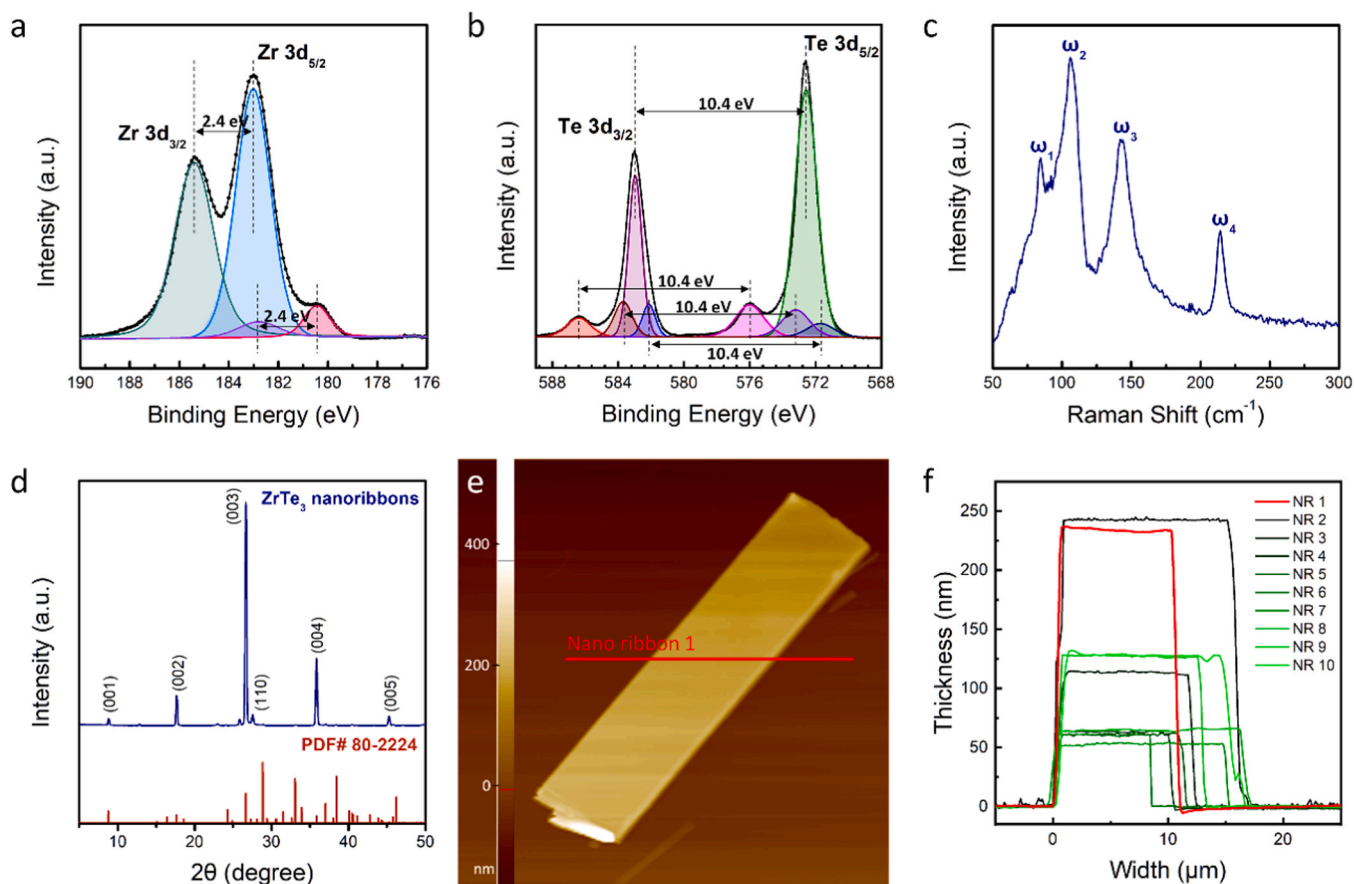


Fig. 2. Characterizations of ZrTe_3 single crystals and nanoribbons. (a) Zr 3d and (b) Te 3d X-ray photoelectron spectra obtained from a ZrTe_3 single crystal. (c) Raman spectrum acquired under 532 nm laser excitation for a ZrTe_3 nanoribbon exfoliated from the single crystal. (d) X-ray diffraction pattern of a ZrTe_3 single crystal. (e) Atomic force microscopy (AFM) topography image of a 236-nm-thick nanoribbon. (f) AFM height profiles of mechanically exfoliated ZrTe_3 nanoribbons.

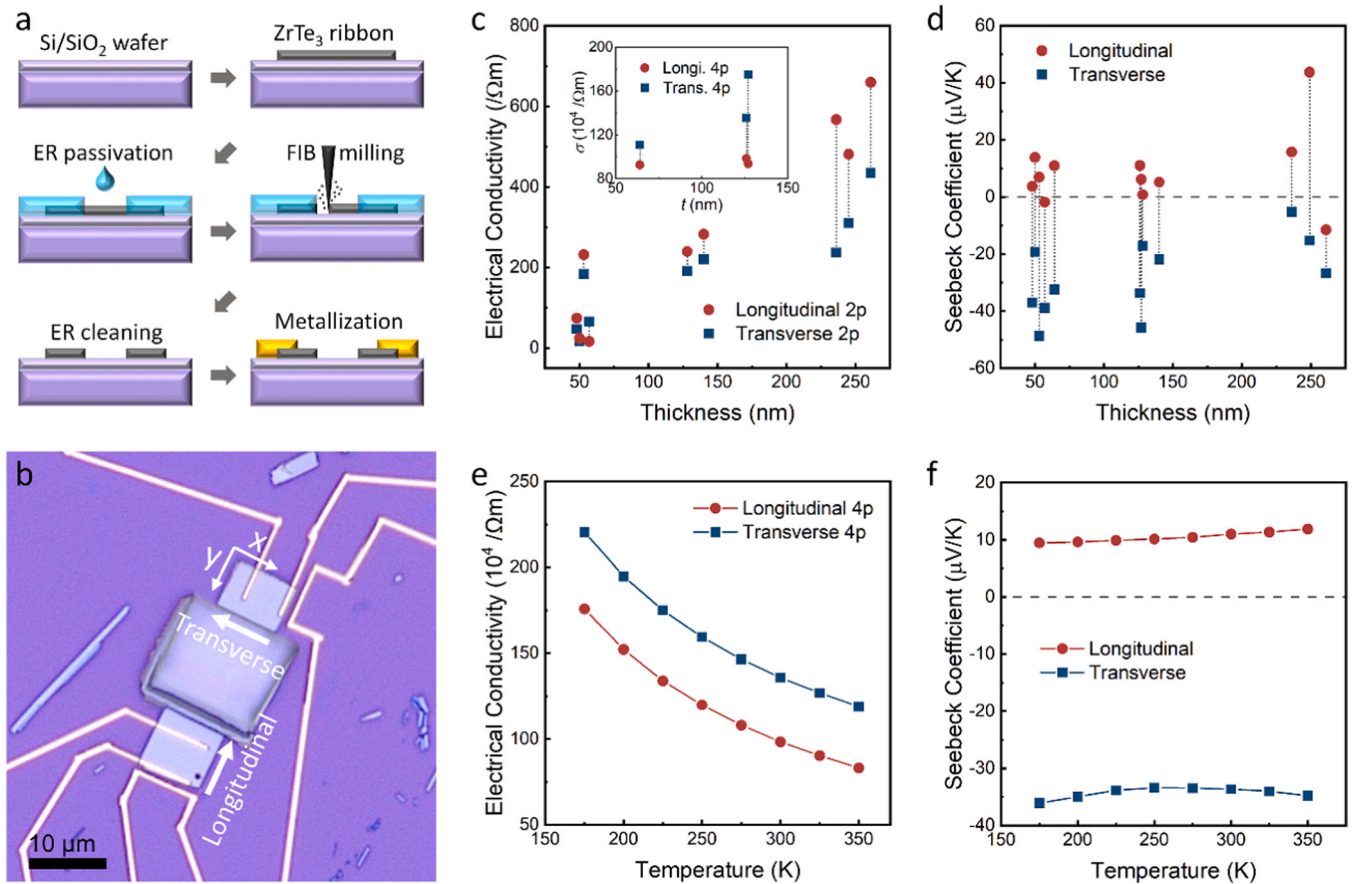


Fig. 3. Anisotropic transport properties of ZrTe₃ nanoribbons. (a) Schematics of device fabrication for the bidirectional measurement using focused ion beam milling with a passivation layer. (b) Microdevices synthesized using a single ZrTe₃ nanoribbon for electrical conductivity and Seebeck coefficient measurements in the longitudinal (y-axis) and transverse (x-axis) directions. (c and d) Room-temperature (c) two-point (2p) electrical conductivities and (d) Seebeck coefficients of ZrTe₃ nanoribbons with various thicknesses ranging from 50 to 260 nm. The four-point (4p) electrical conductivity was depicted in the inset of (c). Dotted lines connecting the longitudinal and transverse values indicate that the pair of values was obtained from a single nanoribbon. (e and f) Temperature dependences of the (e) 4p electrical conductivity and (f) Seebeck coefficient of a ZrTe₃ nanoribbon with a thickness of 128 nm. Error bars were smaller than the symbol size.

beam resist (ER) was used as the passivation layer to prevent unintended damage and contamination of the sample, and electrode metallization and bidirectional measurement were performed (Details of device fabrication are provided in the Experimental section and Fig. S3). Variations of the transport properties caused by FIB milling without ER passivation layer are comprehensively discussed in the Section 2.5. Fig. 3b shows two microdevices based on a single ZrTe₃ nanoribbon for σ and S measurements in the longitudinal and transverse directions (Measurement method is systematically described in the Experimental section and Figs. S4 and S5).

Fig. 3c depicts σ values in the longitudinal and transverse directions obtained from the two-terminal devices of ZrTe₃ nanoribbons with various thicknesses (ranging from 50 to 260 nm) at room temperature. Although a trend is observed in σ corresponding to the thickness reduction, the values obtained based on the two-probe (2p) method include disturbances due to the contact resistance. In particular, this issue is exacerbated in low-dimensional materials, where it is difficult to achieve the sufficient channel length.[39,40] Furthermore, in the nanoribbons used for bidirectional measurement, except for one nanoribbon (57 nm thick), σ in the longitudinal direction was higher than that in the transverse direction, which was contrary to the anisotropy obtained in a previous study conducted on bulk ZrTe₃ crystals.[24] Therefore, the four-probe (4p) method was employed using additional devices with a four-terminal configuration to eliminate the contact resistance and to clearly identify the anisotropy of σ (Fig. S6). All the nanoribbons tested using the 4p method revealed identical anisotropies,

where σ along the transverse direction was higher than that along the longitudinal direction, as shown in inset of Fig. 3c. In a typical MX₃ composed of quasi-1D chains, σ in the chain direction is expected to be higher than that in the perpendicular direction.[37,41] Nevertheless, as ZrTe₃ comprises chains with extensive Te–Te interactions perpendicular to the chain direction, its band structure and Fermi level are substantially dependent on the Te–Te interaction.[24] Therefore, the anisotropy and thickness dependence observed in the 2p method can be attributed to the effect of contact resistance. For the four-terminal devices, the contact resistance was observed to be higher along the transverse direction than that along the longitudinal direction (Fig. S6).

Anisotropy of transport was further clearly obtained in the case of S as compared to that in the case of σ . Generally, S demonstrates strong sensitivity to the variation of intrinsic properties such as carrier density and mobility. Specifically, because the signs of partial S values of an electron and a hole are opposite, the sensitivity of S to the carrier density is significantly high in materials with minor carriers.[9,42,43] Therefore, S definitely reveals the anisotropic transport because of band asymmetry, whereas σ obtained using the 2p method includes uncertainties owing to the contact resistance and shape effect (Fig. S7). Fig. 3d depicts the S values of the ZrTe₃ nanoribbons measured in the longitudinal and transverse directions at room temperature. S values of the ZrTe₃ nanoribbons in the longitudinal directions were mainly positive, whereas these values were negative in the transverse directions for all the samples; these results are in appropriate agreement with those of a previous study on bulk crystals.[24] Although negative longitudinal S

values were acquired for the 57- and 261-nm-thick nanoribbons, stronger *n*-type characteristics were verified along the transverse direction for the same nanoribbons, and the corresponding absolute values were smaller than the transverse values obtained for the other samples. This *n*-type bias can be explained as a non-neutral state with shifted Fermi energy originating from surface oxidation or defects occurring during device fabrication in an atmospheric environment, which has been reported in previous studies on 2D materials.[44–46] The thickness dependence of *S* was insignificant, which is consistent with the previous theoretical calculations that the metallic band characteristics of ZrTe₃ are maintained even in the monolayer.[16]

Fig. 3e and f show σ and *S* of the 126-nm-thick ZrTe₃ nanoribbon as functions of temperature from 175 to 350 K. The temperature dependence of σ was measured using a four-terminal device to exclude the influence of contact resistance that increases with the decrease in temperature (Fig. S6). σ is determined by carrier density and mobility, which are positively and negatively correlated with temperature, respectively.[47,48] Therefore, σ of the nanoribbon, which monotonically increases with a decrease in the temperature for both directions, clearly reflected the metallic band characteristic of ZrTe₃. The transverse σ was maintained at a higher value than that of the longitudinal σ over the entire measured temperature range. *S* of the ZrTe₃ nanoribbon exhibited weak temperature dependences in both directions, as reported in a previous study on bulk crystals (Fig. 3f).[24] Notably, the longitudinal *S* in a nanoribbon changes from positive to negative with a decrease in the temperature; this variation is not observed for bulk crystals (Fig. S8).[24] Variation of longitudinal *S* was clearly confirmed from the Seebeck voltage versus microheater current curves. Considering that sign reversal is accompanied by a slight increase in the absolute value of negative transverse *S*, the *n*-type biases observed in a few samples may also be caused by a decrease in the temperature, indicating that the *S* is highly sensitive to the intrinsic properties (Fig. 3d).

2.4. Theoretical calculations

To theoretically verify the anisotropic transport properties of ZrTe₃ nanoribbons, we calculated the electronic structures and transport properties of ZrTe₃ using the first-principles density functional theory (DFT) calculations and linearized Boltzmann transport equation (Fig. 4). Considering the thicknesses of the nanoribbons used in the transport measurements, the DFT calculations were conducted based on the bulk crystal. Calculated band structure demonstrated both valence and conduction bands in the proximity of the Fermi energy level (Fig. 4a). Overlap between the valence and conduction bands indicated a metallic band structure, which is considerably consistent with the results of

previous theoretical studies (Fig. S9).[16,49] Although the band structure of ZrTe₃ has been sufficiently reported, only a few calculations have been performed on the anisotropic transport properties including σ and *S*. The calculated σ along the longitudinal direction was lower than that in the transverse direction (Fig. 4b). Although the relative magnitude of the calculated σ along both the directions was dependent on the calculation method, this result is consistent with our measurement results (Fig. 3c). It clearly highlights the dependence of the electronic structure on the Te–Te interaction perpendicular to the chain (Fig. S9). In the case of *S* calculation, demonstrating the similar anisotropies identified in ZrTe₃ nanoribbons and bulk crystals was still challenging; however, the energy-dependent variation of *S* similar to our experimental results was possible under certain conditions. Fig. 4c shows the *S* values evaluated at 100, 200, and 300 K as a function of energy. Positive longitudinal and negative transverse *S* values were acquired near the Fermi energy level at low temperature conditions. Furthermore, the *n*-type biases of *S* observed in a few nanoribbon devices were confirmed to occur via a shift of the Fermi energy level (Fig. 3d). Although completely demonstrating the anisotropy of transport observed via experimental measurements using the transport calculations is difficult, the dependence of the sign of *S* on direction in a single material was verified based on the calculated band structure.

2.5. Variation in transport properties and thermoelectric potential

In this study, the initial transport test was conducted using a pristine single nanoribbon for the longitudinal and transverse directions to observe the anisotropic transport of exfoliated ZrTe₃ (Fig. S10a). In the case of *S*, clear observation of the anisotropy was expected because the signs are opposite depending on the direction according to the theoretical calculation and previous studies. However, as two different measurement configurations should be fabricated on a single nanoribbon, generating a uniform temperature gradient throughout the sample for quantitative analysis was challenging. Moreover, extremely high inaccuracy was present even in the qualitative comparison of σ owing to the shape effect of the excessively long length nanoribbon and conduction in the counter electrodes on the same sample. Therefore, as described earlier, we employed FIB milling to divide a single nanoribbon into two pieces, and significant variations in transport properties were observed in the initial tests performed without the ER passivation layer (Fig. 5).

Fig. 5a depicts the schematics of device fabrication and sequential measurements during the initial test, in which the changes in transport properties caused by Ga ion milling were noticed. The selected area on the nanoribbon was milled together with the substrate using 300 pA Ga⁺ beam under the etching condition (500 nm SiO₂) (Fig. 5b). As the

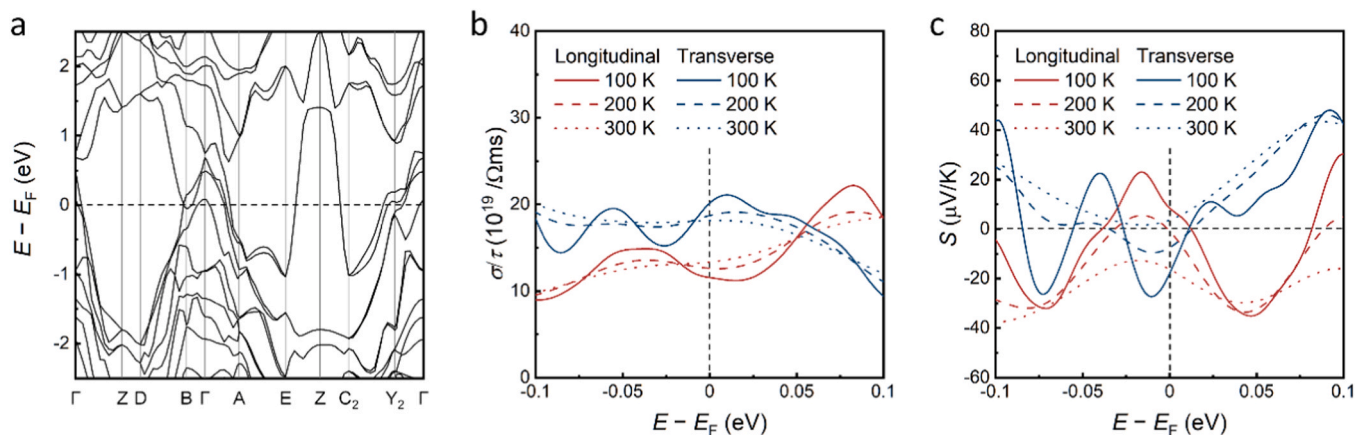


Fig. 4. Theoretical calculations of the electronic properties of ZrTe₃. (a) Electronic band structure of ZrTe₃. (b) Electrical conductivity with respect to the scattering time and (c) Seebeck coefficient of ZrTe₃ as a function of energy.

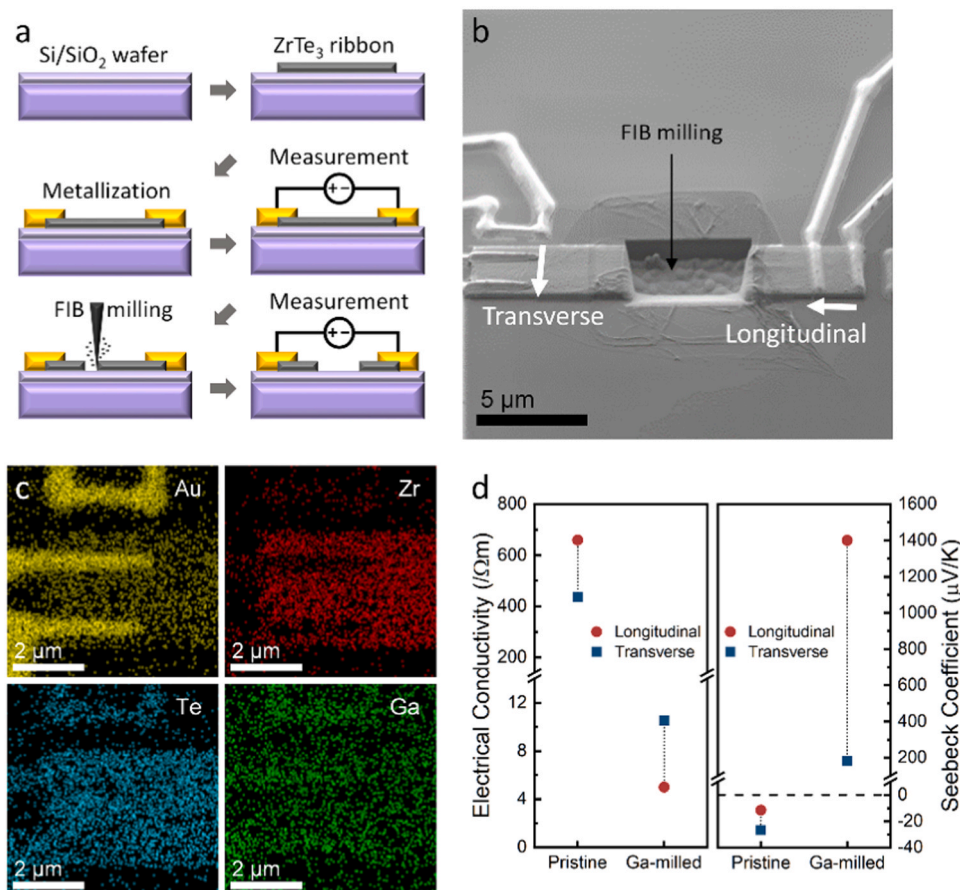


Fig. 5. Variations in the transport properties of the ZrTe₃ nanoribbon caused by focused ion beam (FIB) milling. (a) Schematics of microdevice fabrication and sequential measurements before and after FIB milling without the passivation layer. (b) Scanning electron microscopy image of a ZrTe₃ microdevice milled by selected-area FIB without passivation. (c) Elemental distribution mapping images for Au, Zr, Te, and Ga obtained using the milled microdevice by energy-dispersive X-ray spectroscopy. (d) Changes in the 2p electrical conductivities and Seebeck coefficients in the longitudinal and transverse directions at room temperature induced by FIB milling without sample passivation.

sample was not protected during this process, the contamination caused by FIB milling was clearly observed around the milled area (Fig. S10d). Elemental mapping analysis revealed extensive Ga contamination on the channel at a distance of few micrometers from the milled area (Fig. 5c). Considering the thickness of the nanoribbon (261 nm), an issue of contamination might be present due to the redepositions of the etched substrate components; nevertheless, as the bottom of the nanoribbon was in contact with the substrate, Si was not included in elemental mapping.

Fig. 5d shows the changes in σ and S measured in the longitudinal and transverse directions before and after milling. σ values demonstrated not only severe reductions in both directions, but also reversal of their relative magnitudes. In the case of S , considerable enhancements in the absolute values were obtained in both directions, including the transition from negative to positive S values. These significant variations were evidently observed in the current–voltage (I – V) curves and Seebeck voltage versus heater current curves (Fig. S10). σ and absolute value of S exhibited a trade-off depending on the carrier density according to the Ohm’s law and Mott’s formula, respectively.[50,51] Therefore, the simultaneous changes in two different properties caused by milling indicate a decrease in carrier density. Correlation between these two properties was also revealed in each measurement configuration, in which the direction with higher σ demonstrated lower absolute value of S and vice versa. Furthermore, the abovementioned n - to p -type transition in S implies bipolar transports in ZrTe₃ nanoribbons where electrons and holes coexist. Consequently, the contamination caused by Ga⁺ milling can induce a p -type doping of ZrTe₃ according to the change in

the major carrier that determines the type of total S . [39,52,53] However, the result of transport calculation based on band structure did not exhibit significant S enhancement with a variation of energy. Therefore, partial changes in the band structure arising from the physical post-treatment can also be expected. To confirm the reproducibility and controllability of p -type transition, we chose a nanoribbon device with typical anisotropy (236 nm) (Fig. 3), which was milled with the ER passivation layer before the first measurement, and conducted additional milling under a stronger Ga⁺ beam condition without the passivation. In the second measurement after additional milling, a higher level of p -type shift was achieved (Fig. S11).

In this section, we tried to carefully report the feasibility and extendibility of transport modulation in the anisotropic ZrTe₃ nanoribbons via a post-treatment, and the σ and S variations calculated to be more than 100 times enhancement in terms of the thermoelectric power factor ($\sigma \cdot S^2$), which determines electrical thermoelectric performance; nevertheless, the value was smaller than that of conventional thermoelectric materials. Thus, follow-up studies, such as on thickness optimization, doping control, and transport modulation mechanism, should be performed to demonstrate sufficient enhancements in the thermoelectric properties and to facilitate the applications of these materials.

3. Conclusion

In summary, herein, we examined the in-plane anisotropic transport properties of mechanically exfoliated ZrTe₃ nanoribbons. ZrTe₃ is a layered material composed of trigonal prismatic ZrTe₃ chains, which

exfoliates into rectangular nanoribbons with long length in the chain direction and exhibits quasi-1D transport properties despite its 2D structure. The σ values of the ZrTe_3 rectangular nanoribbons were higher along the transverse direction (normal to chain direction) than those along the longitudinal direction. Interestingly, S values of the ZrTe_3 nanoribbons demonstrated opposite signs depending on the measurement direction. Longitudinal S was positive in most nanoribbons, whereas transverse S was negative, which were consistent with the values obtained for the bulk crystals. Although the theoretical calculations of transport properties based on the electronic band structure partially supported the experimental observation, the anisotropy of S with the opposite signs could be determined. We also reported significant changes in the transport properties during device fabrication for bidirectional measurements. Feasibility and extendibility of transport property modulation were confirmed by an additional test, and we expect that our findings will contribute to the understanding of anisotropic transport in quasi-1D ZrTe_3 and expansion of the application fields of quasi-1D ZrTe_3 .

4. Experimental section

4.1. Sample characterization

ZrTe_3 nanoribbons were mechanically exfoliated from bulk ZrTe_3 single crystals (HQ Graphene) using the typical adhesive tape method (3 M scotch tape) and transferred onto thermally oxidized Si substrates with a SiO_2 (300 nm thickness). Morphologies and thicknesses of the nanoribbons were evaluated using field emission scanning electron microscopy (6701 F, JEOL) and AFM (XE-150, Park Systems). Crystal structures of the nanoribbons were investigated via TEM (JEM-ARM200F NEOARM, JEOL). To observe the cross-sectional atomic arrangement, vertically sliced specimens were acquired using dual-beam FIB (crossbeam 540, ZEISS). Elemental mapping analysis was conducted using TEM-energy-dispersive X-ray spectroscopy (JED-2300T (Dual), JEOL). Surface chemical analyses were performed using analytical tools including a Raman spectrometer with a 532 nm laser (LabRam ARAMIS, Horiba Scientific) and an XPS (K-alpha, Thermo Fisher Scientific, Inc.).

4.2. Device fabrication

Microelectrodes for transport measurement were patterned on the ZrTe_3 nanoribbon on the SiO_2/Si substrate via electron beam lithography (VEGA3, Tescan and NPGS, JC Nabity Lithography Systems) and the standard lift-off process. To enhance the mechanical and electrical contacts between the nanoribbon and electrodes, the patterned window on the nanoribbon was exposed to Ar plasma for 40 s by custom-made plasma etching. Metallization of the patterned electrodes was conducted using Cr (10 nm)/Au (150 nm) by a custom-built magnetron sputtering system. Rectangular nanoribbons transferred onto the substrate were divided into two pieces for the longitudinal and transverse measurements via FIB milling with ER (950 polymethyl methacrylate A4) passivation layer prior to microdevice fabrication (Fig. S3).

4.3. Transport measurements

Transport properties of the ZrTe_3 nanoribbon devices were measured by a microheater and two electrodes using a current source (6221, Keithley) and nanovoltmeter (2182, Keithley) under high-vacuum conditions. Resistance between two electrodes (namely, near and far electrodes) was evaluated using the I - V configuration and converted to σ based on the nanoribbon dimension (Fig. S4). S was obtained by the relation $S = -\Delta V / \Delta T$, where ΔV is the Seebeck voltage measured between the two electrodes and ΔT is the temperature difference generated by Joule heating of the microheater. In typical microdevices employed for the S measurement, ΔT is determined from the temperature

coefficient of resistance of two thermometers (namely, near and far thermometers) with a four-terminal configuration.[9,54] However, in the ZrTe_3 microdevices used for bidirectional measurements, patterning the thermometers with four-terminals is challenging due to the severe step on the side of the nanoribbon induced by FIB milling. Therefore, ΔT values were acquired from dummy devices containing the thermometers (Figs. S4 and S5). Notably, the real S value of the nanoribbons may be approximately 10% higher than the measured value since the ΔT measurement using the dummy sample causes under-estimation of S . Resistance changes of thermometers owing to Joule heating were obtained using a lock-in amplifier (SR850, Stanford Research Systems). All measurements, such as temperature-dependent transport property measurements, were performed using a cryostat system (X-1AL, Advanced Research Systems) under a high-vacuum condition to prevent convectional temperature fluctuation.

4.4. Theoretical calculations

First-principles DFT calculations were performed using the Heyd-Scuseria-Ernzerhof hybrid functional and the projector augmented-wave method, implemented in the Vienna *ab initio* simulation program code.[55–57] The 4 s, 4p, 4d, and 5 s electrons of Zr and 5 s and 5p electrons of Te were used as valence electrons. The plane-wave basis cut-off energy was set to 400 eV. The k -point meshes of $2 \times 3 \times 1$ and $3 \times 7 \times 1$ were employed for structural relaxation and electronic structure calculations, respectively. An electronic self-consistency convergence criterion of 10^{-6} eV was used, and structural relaxation was performed until the Hellmann-Feynman forces reached a convergence threshold of less than 5×10^{-2} eV \AA^{-1} . Transport properties of ZrTe_3 were estimated using the Shankland-Koelling-Wood interpolation as implemented in the BoltzTraP2 code.[58,59] At first, the band structures acquired by DFT calculations were interpolated using the extended Shankland algorithm.[60–62] Thereafter, the Onsager transport coefficients were determined using the linearized Boltzmann transport equation based on the rigid-band approximation.

CRediT authorship contribution statement

Seonhye Youn: Writing – original draft, Investigation, Formal analysis. **Jeongmin Kim,:** Writing – review & editing, Writing – original draft, Investigation, Formal analysis, Conceptualization. **Heejun Lee:** Investigation, Formal analysis. **Dong Hwan Kim:** Formal analysis. **Joonho Bang:** Writing – review & editing, Writing – original draft, Formal analysis, Data curation. **Wooyoung Lee:** Writing – review & editing, Supervision, Funding acquisition.

Declaration of Competing Interest

The authors declare that they have no known competing financial interests or personal relationships that could have appeared to influence the work reported in this paper.

Data Availability

Data will be made available on request.

Acknowledgments

This work was supported by the Technology Innovation Program ('20013621', Center for Super Critical Material Industrial Technology) funded By the Ministry of Trade, Industry & Energy(MOTIE, Korea), and the Basic Science Research Program through the National Research Foundation of Korea (NRF) funded by the Ministry of Education (NRF-2019R1A6A1A11055660). J.K. acknowledges support from the National Research Foundation of Korea (RS-2023-00211034 and NRF-2021R1A5A8033165). J.B. acknowledges support from the National

Research Foundation of Korea (NRF-2022R1C1C2005931).

Appendix A. Supporting information

Supplementary data associated with this article can be found in the online version at doi:10.1016/j.nanoen.2024.109771.

References

- [1] S.Z. Butler, S.M. Hollen, L. Cao, Y. Cui, J.A. Gupta, H.R. Gutiérrez, T.F. Heinz, S. S. Hong, J. Huang, A.F. Ismach, E. Johnston-Halperin, M. Kuno, V.V. Plashnitsa, R. D. Robinson, R.S. Ruoff, S. Salahuddin, J. Shan, L. Shi, M.G. Spencer, M. Terrones, W. Windl, J.E. Goldberger, Progress, challenges, and opportunities in two-dimensional materials beyond graphene, *ACS Nano* 7 (2013) 2898–2926.
- [2] L. Wang, P. Hu, Y. Long, Z. Liu, X. He, Recent advances in ternary two-dimensional materials: synthesis, properties and applications, *J. Mater. Chem. A* 5 (2017) 22855–22876.
- [3] Y. Li, H. Zhu, F. Shen, J. Wan, S. Lacey, Z. Fang, H. Dai, L. Hu, Nanocellulose as green dispersant for two-dimensional energy materials, *Nano Energy* 13 (2015) 346–354.
- [4] E.J.H. Lee, K. Balasubramanian, R.T. Weitz, M. Burghard, K. Kern, Contact and edge effects in graphene devices, *Nat. Nanotechnol.* 3 (2008) 486–490.
- [5] K.S. Novoselov, V.I. Fal'ko, L. Colombo, P.R. Gellert, M.G. Schwab, K. Kim, A roadmap for graphene, *Nature* 490 (2012) 192–200.
- [6] M.J. Allen, V.C. Tung, R.B. Kaner, Honeycomb carbon: a review of graphene, *Chem. Rev.* 110 (2010) 132–145.
- [7] C. Xie, C. Mak, X. Tao, F. Yan, Photodetectors based on two-dimensional layered materials beyond graphene, *Adv. Funct. Mater.* 27 (2017) 1603886.
- [8] L. Sun, C. Chen, Q. Zhang, C. Sohr, T. Zhao, G. Xu, J. Wang, D. Wang, K. Rossnagel, L. Gu, C. Tao, L. Jiao, Suppression of the charge density wave state in two-dimensional 1T-TiSe₂ by atmospheric oxidation, *Angew. Chem. Int. Ed.* 56 (2017) 8981–8985.
- [9] H. Moon, J. Bang, S. Hong, G. Kim, J.W. Roh, J. Kim, W. Lee, Strong thermopower enhancement and tunable power factor via semimetal to semiconductor transition in a transition-metal dichalcogenide, *ACS Nano* 13 (2019) 13317–13324.
- [10] Z. Yu, Z.-Y. Ong, S. Li, J.-B. Xu, G. Zhang, Y.-W. Zhang, Y. Shi, X. Wang, Analyzing the carrier mobility in transition-metal dichalcogenide MoS₂ field-effect transistors, *Adv. Funct. Mater.* 27 (2017) 1604093.
- [11] C. Chiritescu, D.G. Cahill, N. Nguyen, D. Johnson, A. Bodapati, P. Keblinski, P. Zschack, Ultralow thermal conductivity in disordered, layered WSe₂ crystals, *Science* 315 (2007) 351–353.
- [12] S. Kong, T. Wu, M. Yuan, Z. Huang, Q.-L. Meng, Q. Jiang, W. Zhuang, P. Jiang, X. Bao, Dramatically enhanced thermoelectric performance of MoS₂ by introducing MoO₂ nano-inclusions, *J. Mater. Chem. A* 5 (2017) 2004–2011.
- [13] A. Geremew, M.A. Bloodgood, E. Aytan, B.W.K. Woo, S.R. Corber, G. Liu, K. Bozhilov, T.T. Salguero, S. Rummyantsev, M.P. Rao, A.A. Balandin, Current carrying capacity of quasi-1D ZrTe₃ van der Waals nanoribbons, *IEEE Electron Device Lett.* 39 (2018) 735–738.
- [14] M. Chen, L. Li, M. Xu, W. Li, L. Zheng, X. Wang, Quasi-one-dimensional van der Waals transition metal trichalcogenides, *Research* 6 (2023) 0066.
- [15] J. Ma, S. Nie, X. Gui, M. Naamneh, J. Jandke, C. Xi, J. Zhang, T. Shang, Y. Xiong, I. Kapon, N. Kumar, Y. Soh, D. Gosálbez-Martínez, O.V. Yazyev, W. Fan, H. Hübener, U.D. Giovannini, N.C. Plumb, M. Radovic, M.A. Sentef, W. Xie, Z. Wang, C. Mudry, M. Müller, M. Shi, Multiple mobile excitons manifested as sidebands in quasi-one-dimensional metallic TaSe₃, *Nat. Mater.* 21 (2022) 423–429.
- [16] Y. Jin, X. Li, J. Yang, Single layer of MX₃ (M = Ti, Zr; X = S, Se, Te): a new platform for nano-electronics and optics, *Phys. Chem. Chem. Phys.* 17 (2015) 18665–18669.
- [17] J. Dai, X.C. Zeng, Titanium trisulfide monolayer: theoretical prediction of a new direct-gap semiconductor with high and anisotropic carrier mobility, *Angew. Chem. Int. Ed.* 54 (2015) 7572–7576.
- [18] C. Wang, C. Zheng, G. Gao, Bulk and monolayer ZrS₃ as promising anisotropic thermoelectric materials: a comparative study, *J. Phys. Chem. C* 124 (2020) 6536–6543.
- [19] K. Gu, R.A. Susilo, F. Ke, W. Deng, Y. Wang, L. Zhang, H. Xiao, B. Chen, Pressure-induced enhancement in the superconductivity of ZrTe₃, *J. Phys.: Condens. Matter* 30 (2018) 385701.
- [20] Z. Hui, Y. Wang, N. Shen, D. Han, X. Li, J. Gong, Few-layer ZrTe₃ nanosheets for ultrashort pulse mode-locked laser in 1.55 μm region, *Opt. Mater.* 123 (2022) 111939.
- [21] S. Tsuchiya, K. Matsubayashi, K. Yamaya, S. Takayanagi, S. Tanda, Y. Uwatoko, Effects of pressure and magnetic field on superconductivity in ZrTe₃: local pair-induced superconductivity, *N. J. Phys.* 19 (2017) 063004.
- [22] N.V. Morozova, I.V. Korobeynikov, K.V. Kurochka, A.N. Titov, S.V. Ovsyannikov, Thermoelectric properties of compressed titanium and zirconium trichalcogenides, *J. Phys. Chem. C* 122 (2018) 14362–14372.
- [23] S. Takahashi, T. Sambongi, J. Brill, W. Roark, Transport and elastic anomalies in ZrTe₃, *Solid State Commun.* 49 (1984) 1031–1034.
- [24] C. Felser, E. Finckh, H. Kleinke, F. Rucker, W. Tremel, Electronic properties of ZrTe₃, *J. Mater. Chem.* 8 (1998) 1787–1798.
- [25] T. Debnath, B. Debnath, R.K. Lake, Thermal conductivity of the quasi-one-dimensional materials TaSe₃ and ZrTe₃, *Phys. Rev. Mater.* 5 (2021) 034010.
- [26] K. Stöwe, F.R. Wagner, Crystal structure and calculated electronic band structure of ZrTe₃, *J. Solid State Chem.* 138 (1998) 160–168.
- [27] Y. Hu, F. Zheng, X. Ren, J. Feng, Y. Li, Charge density waves and phonon-electron coupling in ZrTe₃, *Phys. Rev. B* 91 (2015) 144502.
- [28] X. Yu, X. Wen, W. Zhang, L. Yang, H. Wu, X. Lou, Z. Xie, Y. Liu, H. Chang, Fast and controlled growth of two-dimensional layered ZrTe₃ nanoribbons by chemical vapor deposition, *CrystEngComm* 21 (2019) 5586–5594.
- [29] A.M. Ganose, L. Gannon, F. Fabrizi, H. Nowell, S.A. Barnett, H. Lei, X. Zhu, C. Petrovic, D.O. Scanlon, M. Hoesch, Local corrugation and persistent charge density wave in ZrTe₃ with Ni intercalation, *Phys. Rev. B* 97 (2018) 155103.
- [30] B. Mortazavi, F. Shojaei, M. Yagmurcukardes, M. Makaremi, X. Zhuang, A theoretical investigation on the physical properties of zirconium trichalcogenides, ZrS₃, ZrSe₃ and ZrTe₃ monolayers, *Energies* 15 (2022) 5479.
- [31] S. Furuseth, H. Fjellvåg, Reexamination of the crystal-structure of ZrTe₃, *Acta Chem. Scand.* 45 (1991) 694–697.
- [32] S. Furuseth, L. Brattas, A. Kjekshus, Crystal structures of TiS₃, ZrS₃, ZrSe₃, ZrTe₃, HfS₃ and HfSe₃, *Acta Chem. Scand.* 29 (1975) 623.
- [33] P. Wang, N.-C. Zhang, C.-L. Jiang, F.-S. Liu, Z.-T. Liu, Q.-J. Liu, Structural, mechanical, and electronic properties of Zr-Te compounds from first-principles calculations, *Chin. Phys. B* 29 (2020) 076201.
- [34] C. Yadav, P. Paulose, Superconductivity at 5.2 K in ZrTe₃ polycrystals and the effect of Cu and Ag intercalation, *J. Phys.: Condens. Matter* 24 (2012) 235702.
- [35] Y. Liu, Z. Hu, X. Tong, D. Leshchev, X. Zhu, H. Lei, E. Stavitski, K. Attenkofer, C. Petrovic, Thermal transport and mixed valence in ZrTe₃ doped with Hf and Se, *Appl. Phys. Lett.* 120 (2022).
- [36] J. Qiao, S. Ahmed, P.K. Cheng, R. Fan, A.M. Saleque, M.N.A.S. Ivan, J. Yu, G. Liu, S. Feng, Y.H. Tsang, Nonlinear optical properties and broadband ultrafast photonics application of 2D-zirconium tritelluride (ZrTe₃), *Opt. Laser Technol.* 158 (2023) 108849.
- [37] J. Jin, M. Wurch, S. Baraghani, D.J. Coyle, T.A. Empante, F. Kargar, A.A. Balandin, L. Bartels, Metallic transport in chemical vapor deposition ZrTe₃ nanoribbons on a SiO₂ wafer substrate, *Cryst. Growth Des.* 21 (2021) 6537–6542.
- [38] X. Zhu, B. Lv, F. Wei, Y. Xue, B. Lorenz, L. Deng, Y. Sun, C.-W. Chu, Disorder-induced bulk superconductivity in ZrTe₃ single crystals via growth control, *Phys. Rev. B* 87 (2013) 024508.
- [39] J. Kim, S. Lee, Y.M. Brovman, P. Kim, W. Lee, Diameter-dependent thermoelectric figure of merit in single-crystalline Bi nanowires, *Nanoscale* 7 (2015) 5053–5059.
- [40] S. Yoo, J. Kim, H. Moon, S.Y. Kim, D.-s. Ko, W.H. Shin, S. Hwang, D.W. Jung, S. Sul, C. Kwak, Strong enhancement of electrical conductivity in two-dimensional micrometer-sized RuO₂ nanosheets for flexible transparent electrodes, *Nanoscale* 9 (2017) 7104–7113.
- [41] A. Jain, S.P. Ong, G. Hautier, W. Chen, W.D. Richards, S. Dacek, S. Cholia, D. Gunter, D. Skinner, G. Ceder, Commentary: The Materials Project: a materials genome approach to accelerating materials innovation, *APL Mater.* 1 (2013).
- [42] H. Moon, J. Kim, J. Bang, S. Hong, S. Youn, H. Shin, J.W. Roh, W. Shim, W. Lee, Semimetallic features in thermoelectric transport properties of 2H–3Br phase niobium diselenide, *Nano Energy* 78 (2020) 105197.
- [43] J. Heremans, C. Thrush, Thermoelectric power of bismuth nanowires, *Phys. Rev. B* 59 (1999) 12579.
- [44] J. Kim, S. Youn, J. Bang, H. Moon, W. Jang, J.W. Roh, D.H. Kim, J. Chang, W. Lee, Experimental verification of semimetallic band structure in PtSe₂ via thermoelectric power measurements, *Appl. Phys. Lett.* 120 (2022).
- [45] D. Kong, J.J. Cha, K. Lai, H. Peng, J.G. Analytis, S. Meister, Y. Chen, H.-J. Zhang, I. R. Fisher, Z.-X. Shen, Rapid surface oxidation as a source of surface degradation factor for Bi₂Se₃, *ACS nano* 5 (2011) 4698–4703.
- [46] D. Cao, H. Shu, T. Wu, Z. Jiang, Z. Jiao, M. Cai, W. Hu, First-principles study of the origin of magnetism induced by intrinsic defects in monolayer MoS₂, *Appl. Surf. Sci.* 361 (2016) 199–205.
- [47] R.-z. Zhang, C.-l. Wan, Y.-f. Wang, K. Koumoto, Titanium sulphene: two-dimensional confinement of electrons and phonons giving rise to improved thermoelectric performance, *Phys. Chem. Chem. Phys.* 14 (2012) 15641–15644.
- [48] Y. Gong, Z. Lin, Y.-X. Chen, Q. Khan, C. Wang, B. Zhang, G. Nie, N. Xie, D. Li, Two-dimensional platinum diselenide: synthesis, emerging applications, and future challenges, *Nano-Micro Lett.* 12 (2020) 1–34.
- [49] M. Abdulsalam, D.P. Joubert, Structural and electronic properties of MX₃ (M = Ti, Zr and Hf; X = S, Se, Te) from first principles calculations, *Eur. Phys. J. B* 88 (2015) 1–11.
- [50] J. Kim, W. Shim, W. Lee, Bismuth nanowire thermoelectrics, *J. Mater. Chem. C* 3 (2015) 11999–12013.
- [51] S. Youn, J. Kim, H. Moon, J.K. Kim, J. Jang, J. Chang, T. Lee, K. Kang, W. Lee, Enhanced thermoelectric power factor in carrier-type-controlled platinum diselenide nanosheets by molecular charge-transfer doping, *Small* 18 (2022) 2200818.
- [52] F. Sarcan, N.J. Fairbairn, P. Zotev, T. Severs-Millard, D.J. Gillard, X. Wang, B. Conran, M. Heuken, A. Erol, A.I. Tartakovskii, Understanding the impact of heavy ions and tailoring the optical properties of large-area monolayer WS₂ using focused ion beam, *npj 2D Mater. Appl.* 7 (2023) 23.
- [53] P. Mishra, M. Tangi, T.K. Ng, M.N. Hedhili, D.H. Anjum, M.S. Alias, C.-C. Tseng, L.-J. Li, B.S. Ooi, Impact of N-plasma and Ga-irradiation on MoS₂ layer in molecular beam epitaxy, *Appl. Phys. Lett.* 110 (2017).
- [54] J. Kim, G. Kim, J.-H. Bahk, J.-S. Noh, W. Lee, Enhanced thermoelectric properties in Bi/Te core/shell heterostructure nanowires through strain and interface engineering, *Nano Energy* 32 (2017) 520–525.
- [55] P.E. Blöchl, Projector augmented-wave method, *Phys. Rev. B* 50 (1994) 17953.
- [56] G. Kresse, J. Furthmüller, Efficient iterative schemes for ab initio total-energy calculations using a plane-wave basis set, *Phys. Rev. B* 54 (1996) 11169.

- [57] A.V. Krukau, O.A. Vydrov, A.F. Izmaylov, G.E. Scuseria, Influence of the exchange screening parameter on the performance of screened hybrid functionals, *J. Chem. Phys.* 125 (2006).
- [58] W.E. Pickett, H. Krakauer, P.B. Allen, Smooth Fourier interpolation of periodic functions, *Phys. Rev. B* 38 (1988) 2721.
- [59] G.K. Madsen, J. Carrete, M.J. Verstraete, BoltzTraP2, a program for interpolating band structures and calculating semi-classical transport coefficients, *Comput. Phys. Commun.* 231 (2018) 140–145.
- [60] R. Euwema, D. Stukel, T. Collins, J. DeWitt, D. Shankland, Crystalline interpolation with applications to Brillouin-zone averages and energy-band interpolation, *Phys. Rev.* 178 (1969) 1419.
- [61] D. Shankland, Fourier transformation by smooth interpolation, *Int. J. Quantum Chem.* 5 (1971) 497–500.
- [62] D. Koelling, J. Wood, On the interpolation of eigenvalues and a resultant integration scheme, *J. Comput. Phys.* 67 (1986) 253–262.